Solar Energy Materials & Solar Cells 305 (2026) 114431

Contents lists available at ScienceDirect

Solar Energy Materials and Solar Cells

journal homepage: www.elsevier.com/locate/solmat

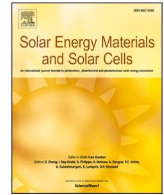

Energy-dependent increase in D_{it} and larger capture cross sections drive UV-induced degradation

Jiaxin Yang [*], Muhammad Umair Khan, Xinyuan Wu, Chandany Sen, Jessica Yajie Jiang, Bram Hoex [**], Fiacre Rougieux [***]

School of Photovoltaic and Renewable Energy Engineering, University of New South Wales, Sydney, Australia

A B S T R A C T

Ultraviolet-induced degradation (UVID) is a significant challenge for high-efficiency commercial silicon solar technology. While prior studies have established that UVID degrades surface passivation and is strongly linked to hydrogen-related processes, the interplay between chemical, electronic, and structural effects at the interface remains incompletely understood. In this work, we extend existing frameworks by combining cell-level observations with a quantitative, energy-resolved analysis of interface defect states and their coupling to field-effect passivation. Initially, we evaluate UVID at the cell level and observe that UV exposure induces pronounced degradation on both the front and rear surfaces of PERC solar cells, as well as on the front surface of TOPCon solar cells, whereas no measurable degradation is observed on the rear surface of TOPCon cells. To analyze the underlying mechanisms, we focus on industrial AlO_x-passivated lifetime samples without a capping SiN_x:H layer and demonstrate that the AlO_x/crystalline silicon (c-Si) interface undergoes degradation under UV exposure. This work focuses on the quantitative analysis of the energy-dependent interface defect density (D_{it}), and UV light increases D_{it} while simultaneously enhancing field-effect passivation by increasing negative fixed charge (Q_f). The combined increase in D_{it} and Q_f ultimately governs the observed reduction in carrier lifetime of AlO_x-passivated samples. By combining Gaussian-distribution modelling of the D_{it} with physical-based lifetime modelling, we demonstrate that UVID is driven by enhanced surface recombination associated with the activation of interface defect states, together with an increase in negative Q_f. This physical perspective offers deeper insight into the full degradation mechanism, complementing existing chemical models.

1. Introduction

Recent studies have increasingly reported that UVID has emerged as a non-negligible reliability issue in advanced silicon solar cell technologies, particularly for TOPCon technology [1], [2], [3], [4], with reports that n-type TOPCon and HJT modules generally exhibit higher and more variable UV susceptibility than PERC modules [5]. This growing concern has coincided with significant changes in module encapsulation strategies over the past few years, including the widespread adoption of UV-transparent encapsulants to enhance energy yield [6], [7], [8]. Unlike conventional UV-blocking materials, UV-transparent encapsulants intentionally transmit or convert UV photons, thereby increasing the UV dose reaching the cell surface and increasing the initial module performance. This increased exposure to UV radiation introduces new challenges to various advanced silicon solar cell technologies [9], including PERC, TOPCon, and heterojunction technology (HJT) [1], [2], [3], [10], [11], as UV exposure can degrade cell performance and induce instabilities of silicon solar cells [1].

Whilst UV degradation has been studied in detail in the past [11], [12], [13], [14], [15], Thome et al. found that TOPCon cells are more sensitive to UV radiation, experiencing a relative degradation in efficiency of more than 7%, with the loss of open-circuit voltage (V_{OC}) being the main reason for this [1]. Khan et al. revealed that both UVA (315-420 nm) and UVB (250-385 nm) irradiation led to the same type of surface degradation in TOPCon solar cells, although the degradation progresses significantly more rapidly under UVB exposure. Moreover, their study demonstrated that UV exposure strongly affects hydrogen redistribution, suppressing light and elevated temperature-induced degradation (LeTID) and increasing hydrogen accumulation at the AlO_x/Si interface, which plays a central role in UVID mechanisms [4]. Recent studies on industrial HJT modules indicate that UVID is a critical reliability concern, where UV exposure can cause power loss mainly through reduced short-circuit current [16]. Razzaq et al. demonstrated that high temperatures can effectively alleviate UVID in HJT solar cells [3]. Their study also indicated that while short-term UVID of HJT cells is largely reversible, prolonged UV radiation causes irreversible defects,

* Corresponding author.
** Corresponding author.
*** Corresponding author.
E-mail addresses: jiaxin.yang1@student.unsw.edu.au (J. Yang), b.hoex@unsw.edu.au (B. Hoex), fiacre.rougieux@unsw.edu.au (F. Rougieux).

https://doi.org/10.1016/j.solmat.2026.114431
Received 31 March 2026; Received in revised form 6 May 2026; Accepted 7 May 2026
0927-0248/© 2026 Published by Elsevier B.V.

resulting in only partial recovery of device performance upon subsequent annealing.

UV exposure can induce multiple degradation mechanisms in silicon solar cells, particularly affecting surface passivation layers. UV radiation with photon energies exceeding approximately 3.4 eV is sufficient to break silicon–hydrogen (Si–H) bonds [17], releasing atomic hydrogen and increasing the silicon dangling bond density. Silicon dangling bonds and excess hydrogen at the interface increase the D_{it}, thereby increasing recombination [18]. A recent work showed that UV stability in c-Si PV modules is strongly interface-dependent, where AlO_x/SiN_x stack with p^+-type emitter remained stable after 598 kWh/m^2 UV exposure, whereas SiN_x layer on the n^+-Si BSF layer caused a 15% power loss due to increased surface recombination. This degradation is attributed to UV-induced surface passivation deterioration, with photons above 3.4 eV increasing the front surface recombination current density [19]. As the primary surface passivation layer at the front of TOPCon and rear of PERC solar cells, AlO_x layer plays a decisive role in determining the overall passivation quality of the silicon surface. Previous studies focusing on the effect of AlO_x thickness under UV irradiation have revealed that a thicker AlO_x layer can effectively suppress UVID, thereby enhancing the long-term stability of silicon solar cells [2]. Gielis et al. (2008) systematically investigated the Q_f characteristics and photon-induced charging dynamics of AlO_x/Si structures using second-harmonic generation (SHG). Their work demonstrates that AlO_x films can increase their negative Q_f density by trapping excited electrons from the underlying c-Si. These results establish AlO_x as a charge-active dielectric whose electrical properties can change under light exposure [20]. Veith-Wolf et al. demonstrated that c-Si symmetrically passivated by fired AlO_x and AlO_x/SiN_x stacks exhibited no degradation under UVA exposure. In contrast, samples symmetrically passivated by SiN_x layers showed a strong degradation. The observed stability of the AlO_x and AlO_x/SiN_x passivated samples was attributed to the increase in negative Q_f density being more than sufficient to compensate for the increase in $D_{it,}$ resulting in the passivation layer/stack being UV stable [21]. Khan et al. developed a comprehensive UVID model for TOPCon passivation stacks. UV exposure was shown to rapidly increase the negative Q_f density, with this additional charge gradually relaxing in the absence of UV illumination (e.g., under dark conditions). As a higher Q_f improves passivation, this results in a temporary boost in passivation. The observed increase in D_{it} was attributed to the breaking of Si–H bonds at the c-Si/AlO_x interface and the SiN_x layer, with elevated interfacial hydrogen concentrations promoting defect formation. This hydrogen can be removed through dark annealing, which restores D_{it} to its initial level. The authors further demonstrated that increasing the AlO_x thickness results in lower D_{it}, an effect attributed to the hydrogen-barrier properties of AlO_x [18].

Most prior work attributes UVID to hydrogen-related processes and photon-induced charging but does not resolve where in the bandgap the interface-state density increases, nor whether the associated change in charge is sufficient to counteract the recombination activity of the newly created interface states. As a result, it remains unclear why industrial cells show a strong dependence on surface characteristics (e.g., diffused vs. undiffused).

To address this, we investigate the physics of UVID in two leading PV technologies (TOPCon and PERC) and study the evolution of charge and energy-dependent D_{it} on symmetrical lifetime structures passivated with commercially used AlO_x film. This novelty of work lies in combining experimental degradation analysis with quantitative interface-defect modelling to reveal the physical origin of UVID in silicon solar cells. Our findings reveal distinct degradation behaviours between two cell architectures and demonstrate that UV irradiation increases charge and D_{it}, with reduced chemical passivation from increased D_{it} counterbalancing the increased field-effect passivation from increased charge. From a modelling perspective, we introduce an energy-dependent defect distribution and capture-cross-section framework to quantitatively reproduce the measured injection-dependent lifetime behaviour. We also show that UVID redistributes interface defect states in energy from a square U-shape distribution to a more rounded distribution.

2. Methodology

Industrial bifacial p-type PERC and n-type TOPCon solar cells with a size of 182 mm × 182 mm, were studied in this paper. For PERC solar cells, a p-type gallium-doped Si substrate was used, and the front side consists of an n-emitter doped with phosphorus, a hydrogenated silicon nitride layer (SiN_x:H), and an H-pattern silver paste on the front side. The rear side consists of a surface stack of aluminium oxide (AlO_x), deposited by atomic layer deposition (ALD), and hydrogenated silicon nitride (SiN_x:H) grown by plasma-enhanced chemical vapour deposition (PECVD). The rear metallisation was formed using an aluminium (Al) grid. The front side of the TOPCon solar cells consists of a boron-doped emitter (p^+ emitter), a surface stack of aluminium oxide (AlO_x) deposited by ALD, a PECVD hydrogen-passivated silicon nitride (SiN_x:H), and H-pattern silver (Ag) paste printing on the front surface. The rear side comprises a silicon dioxide (SiO_2), phosphorus-doped poly-Si/SiN_x:H stack with a H-pattern silver grid. A schematic diagram of the PERC and TOPCon cell is shown in Fig. 1 (a) and 1 (b), respectively. AlO_x symmetric lifetime samples were 182 mm × 182 mm wafers provided by an industrial partner, the substrate was n-type silicon, and an AlO_x layer with a thickness of 9~12 nm was deposited on the front and back side, respectively, using ALD. Symmetric lifetime samples of AlO_x were fired at low temperature (780 °C). Although industrial silicon solar cells typically employ an AlO_x/SiN_x passivation stack, this work deliberately focuses on AlO_x-only structures. This approach enables isolation of the intrinsic UVID mechanisms at the AlO_x/c-Si interface, without the confounding effects of UV absorption, hydrogen redistribution introduced by the SiN_x layer. Importantly, the AlO_x layers investigated in this study were deposited by and industrial ALD processes and subjected to standard firing conditions, ensuring direct relevance to commercial solar cell manufacturing.

The samples were divided into three groups (Group A, B and C), as shown in Fig. 2. They were cut into 40 mm × 40 mm tokens from the back side using a FOBA-M1000 Laser tool to facilitate initial data measurements. Subsequently, the small tokens were placed in a temperature-controlled UV-B chamber with UV lamps with a spectrum between 280 and 385 nm. The UVB irradiance density and hotplate temperature were set to around 114 W/m^2 and 60 °C, respectively. The UV light dose was determined by the UV irradiance and exposure time in the UV-B chamber [4]. Fig. 2 illustrates the experimental design process. The front and back sides of the PERC and TOPCon cells were subjected to UVB exposure experiments, while a control group of samples underwent dark annealing (60 °C) experiments to monitor the effect of temperature on the cells. For AlO_x samples, wafers were irradiated with UVB light and tested for PL images, lifetime, and D_{it} data before and after UV irradiation.

PL images were obtained by using a BTi-R3 imaging tool at room temperature and 1 sun to evaluate the degradation behaviour of cells. PL image analysis was conducted using LumiTools to ensure consistent image scaling [22]. To generate the PL ratio images, the PL images obtained prior to UV exposure was divided by the corresponding post-exposure PL images, measured under the same illumination and camera conditions. In this representation, brighter areas with higher PL ratio values correspond to regions that experienced more degradation. The minority carrier lifetime of the symmetrical AlO_x passivated wafers (Group C) was measured using a WCT-120 lifetime tester (Sinton Instruments, Boulder, CO, USA) based on the quasi-steady-state photoconductance (QSSPC) method. Measurements were conducted under standard conditions at room temperature (25 ± 2 °C), with an excess carrier density of approximately 5×10^{15} cm^{-3} [23]. The effective minority carrier lifetime was measured in generalized mode, with intrinsic recombination effects corrected using the Richter model [24]. The D_{it} of the Group C was characterized by using a corona-oxide characterization

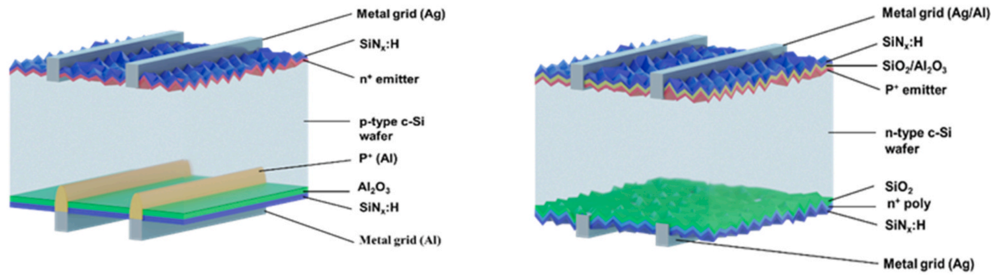

Fig. 1. Structure of (a) bifacial PERC cells; (b) bifacial TOPCon cells.

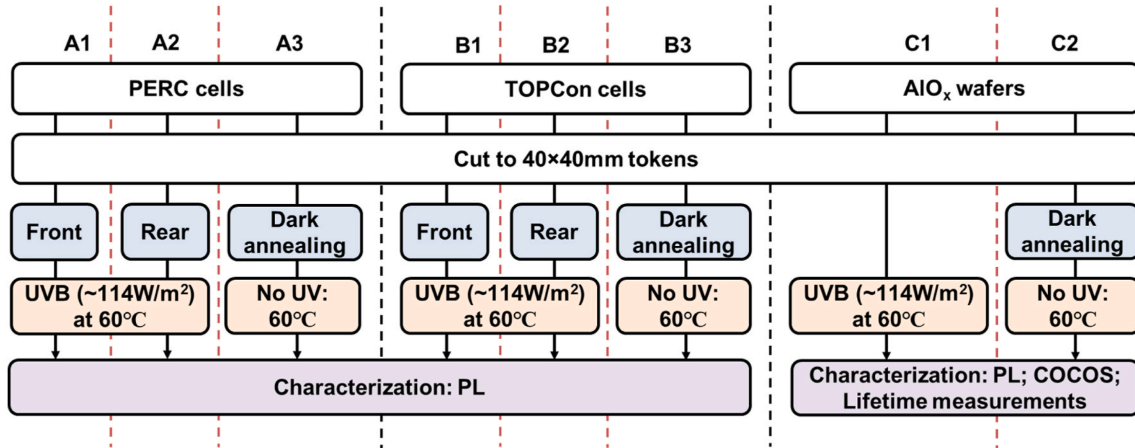

Fig. 2. Experimental flow diagram of this study.

of semiconductor (COCOS) system (SEMILAB PV-2000A). The COCOS technique enables non-contact capacitance–voltage (C–V) profiling by depositing a corona charge and measuring the surface potential, allowing extraction of D_{it} across the bandgap [25]. The measurements were performed at room temperature (25 ± 2 °C) under ambient conditions.

We employ a method that correlates PL counts of cells with saturation current density (J_0), enabling the derivation of a quantitative relationship between the J_0 of cells and PL intensity. The relationship between the measured PL signal and the V_{OC} can be described by the following expression [26]:

$$I_{PL} = Cexp\left(\frac{qVoc}{kT}\right) \quad (1)$$

where I_{PL} is the PL intensity, C is a proportionality constant incorporating the system sensitivity and the probability of photon escape from the sample, q is the elementary charge, k is Boltzmann's constant and T is the temperature.

J_0 was determined using the one-diode relation at open circuit [27].

$$J = J_{SC} - J_0\left(exp\frac{V}{kT/q} - 1\right) \quad (2)$$

Assuming $V \gg kT/q$, the -1 term can be neglected, yielding:

$$J_0 \approx J_{SC} \exp\left(-\frac{qV}{nkT}\right) \quad (3)$$

where J_{SC} is the short-circuit current density and n is the diode ideality factor. This approach provides an effective J_0 that enables consistent comparison of recombination changes across conditions under identical PL acquisition settings.

3. Results and discussion

3.1. UV-induced degradation in silicon solar cells

Fig. 3 shows PL images of Group A subjected to different conditions: (a) UV irradiation on the front side (A1), (b) UV irradiation on the rear side (A2), and (c) dark annealing treatment (A3) as a control group. Comparative analysis of PL images shows a significant degradation in luminescence intensity for cells irradiated on the front and rear sides when exposed to UVB irradiance, and a negligible change in the dark-annealed samples, indicating thermal stability of PERC cells in the absence of UV exposure. From the PL intensity ratio images, it is obvious A1 and A2 are brighter than A3, indicating more pronounced degradation in those areas. Therefore, both the front side and the rear side of PERC cells are sensitive to UV irradiation, and the front side, which is passivated by a single SiN_x film, experienced the strongest degradation.

For Group B, the front surface (B1) is sensitive to UVB exposure. As illustrated in Fig. 4, a pronounced degradation in PL intensity is observed on B1 after UV exposure, indicating significant performance deterioration. In contrast, the rear side of the cells (B2) subjected to the same UV exposure shows minimal changes, suggesting relative stability. This is because the rear side of the TOPCon cell contains a poly-Si passivation layer, which absorbs a significant portion of the UV radiation, thereby reducing the rear-side sensitivity to UV exposure and improving its stability [4].

Furthermore, the results for PERC and TOPCon cells indicate that temperature alone is not a dominant factor in the observed degradation. These observations lead to the clear conclusion that UVID arises on each surface where the c-Si/dielectric interface is exposed to UV irradiation. Therefore, both front and rear sides of PERC cells show degradation after UV exposure; and the AlO_x/SiN_x passivation stack on the TOPCon front surface is strongly affected by UV exposure, whereas the rear side shows no noticeable UVID because the n-poly layer absorbs most of the

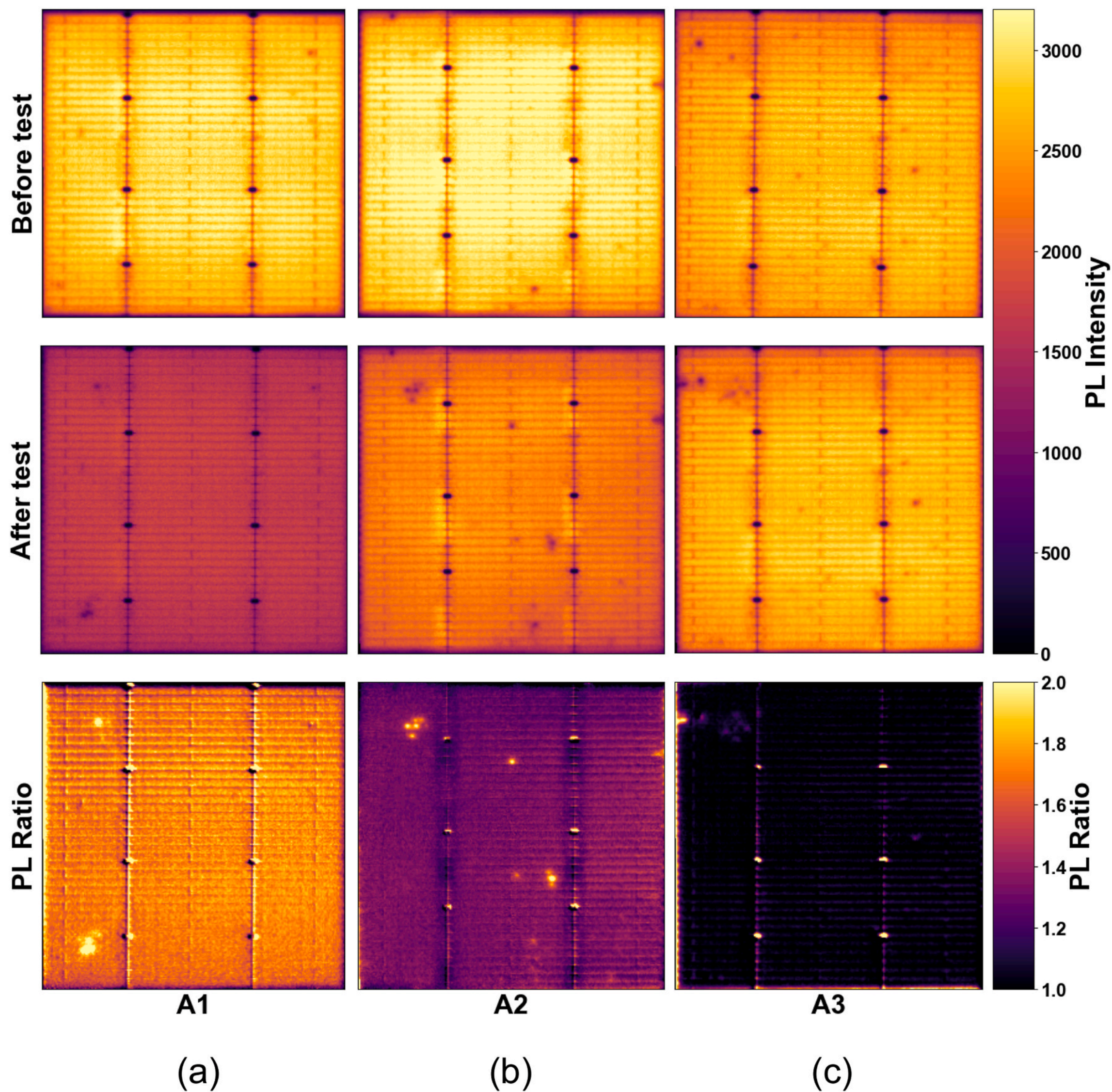

Fig. 3. PL images of Group A after: (a) 20 h of UV exposure (A1), (b) 20 h of UV exposure (A2), (c) 20 h of dark annealing (A3). Brighter regions in PL ratio images correspond to a greater reduction in PL intensity. The PL ratio is defined as $I_{PL,initial}/I_{PL,\ after\ treatment}$.

incident UV radiation.

Fig. 5 illustrates the J_0 trend of Group A and Group B after UVB exposure, with J_0 calculated by Eq. (3). As shown evident in Fig. 5, both PERC and TOPCon cells remain stable under dark annealing conditions. Under UV exposure, however, the PERC cell exhibits a substantial increase in J_0 on both the front and rear sides, indicating a high sensitivity to UV light, with J_0 values increasing by 50-60 (front) and 20-30 (rear) fA/cm^2, respectively, after 20 h of UVB exposure. In contrast, the TOPCon cell shows a pronounced degradation only on the front side with an increase in J_0 of around 20 fA/cm^2 after 20 h of UVB exposure, while the rear sides remain nearly unaffected, which is also consistent with the findings reported by Khan et al. [4]. The J_0 of the TOPCon cell exposed to UV light on the rear remained constant throughout the 20-h testing period, underscoring the superior UV stability of the rear passivation structure. Khan et al. compared identical AlO_x/SiN_x stacks and found that the increase in J_0 was higher on a p^+ surface compared to an un-diffused *n*-type surface, similar as was found here in the case of the n^+ and undiffused *p*-type surface, though in this case the passivation layers were not identical [4], [28]. Optics can not explain this as the rear surface of PERC has a higher reflectance than the front in the UV by only 10-20% [1]. This modest difference cannot account for the much larger degradation observed at the PERC front. Instead, understanding the response requires a deeper understanding of how UV exposure modifies field effect passivation and chemical passivation and how these translate to differences in surface recombination. The next section thus looks at the evolution of charge and interface defect density after UVB radiation.

3.2. UV-induced degradation in AlO_x lifetime test structures

The solar cell results presented above demonstrate that UVID is associated with the dielectric interface/c-Si interface, with its severity dictated by the degree of UV exposure. While the rear interface in TOPCon devices is effectively protected by the poly-Si passivating contact, the front interface of PERC cells remains highly vulnerable, leading to the most significant degradation. In order to better understand how UV exposure influences field effect passivation (via charge) and chemical passivation (via D_{it}) and how these translates into surface recombination, the following section focuses on lifetime test structures using AlO_x passivation to isolate the intrinsic effects of UV exposure on the AlO_x/c-Si interface. It should be noted that the AlO_x-only passivated wafers used in this work are simplified structures designed to isolate the UV response of the AlO_x/c-Si interface. Industrial PERC and TOPCon

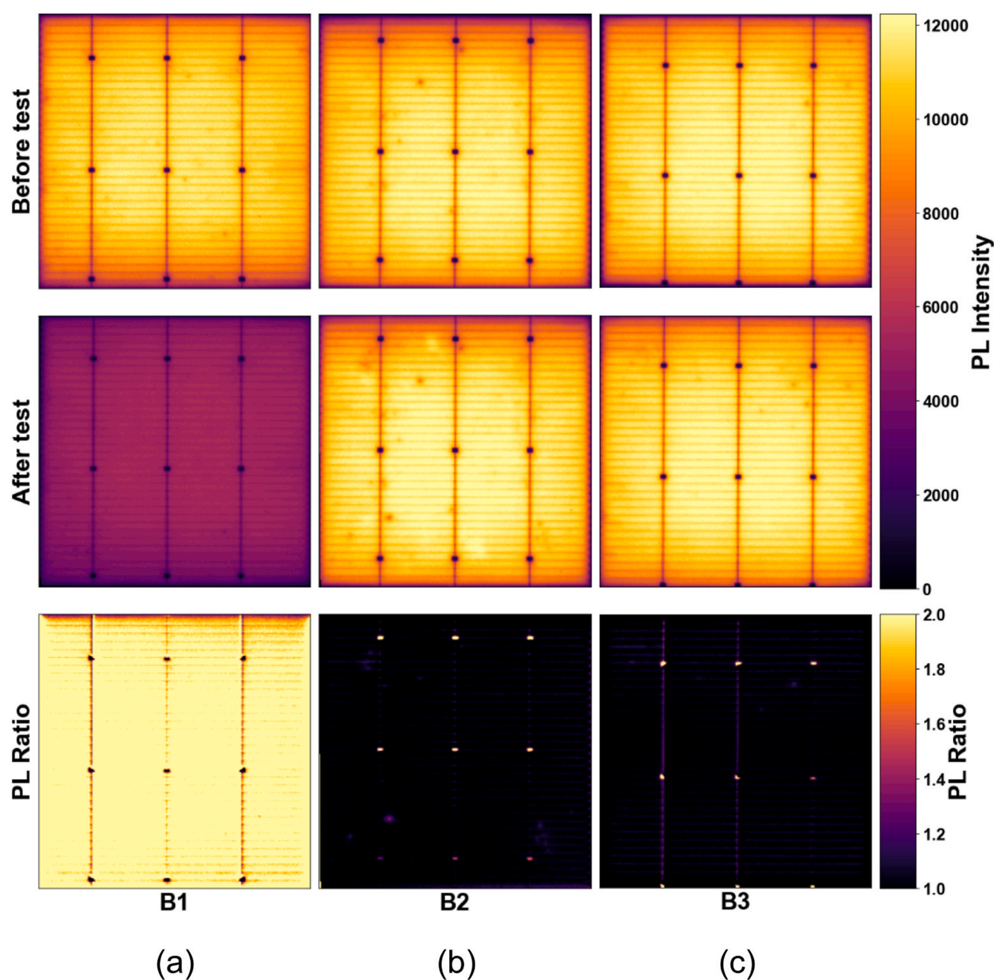

Fig. 4. PL images of Group B after: (a) 20 h of UV exposure (B1), (b) 20 h of UV exposure (B2), (c) 20 h of dark annealing (B3). Brighter regions in PL ratio images correspond to a greater reduction in PL intensity. The PL ratio is defined as $I_{PL,initial}/I_{PL,\ after\ treatment}$.

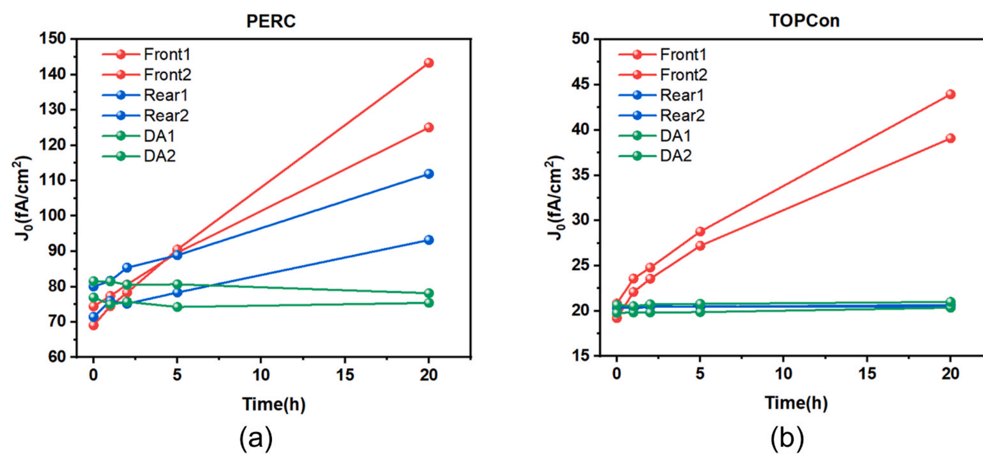

Fig. 5. J_0 of front UV exposure, rear exposure and dark annealing time: (a) bifacial PERC cells, (b) bifacial TOPCon cells.

cells typically employ AlO_x/SiN_x stacks, where the SiN_x capping layer can affect UV transmission, hydrogen availability, hydrogen transport, and charge stability. Therefore, the degradation magnitude observed in AlO_x-only structures should not be directly interpreted as the absolute degradation expected in complete industrial stacks. Nevertheless, the present results remain relevant because they reveal how UV exposure modifies the underlying AlO_x/c-Si interface through coupled changes in interface defect density and fixed-charge density.

Specifically, this study examines changes in PL intensity, D_{it}, Q_f dynamics of symmetrically AlO_x passivated c-Si samples after UVB irradiation. The resulting PL images are presented in Fig. 6, providing insight into the degradation mechanisms induced by prolonged UV exposure. The PL images reveal a pronounced degradation in the Group C samples following UVB irradiation, with the PL intensity decreasing by

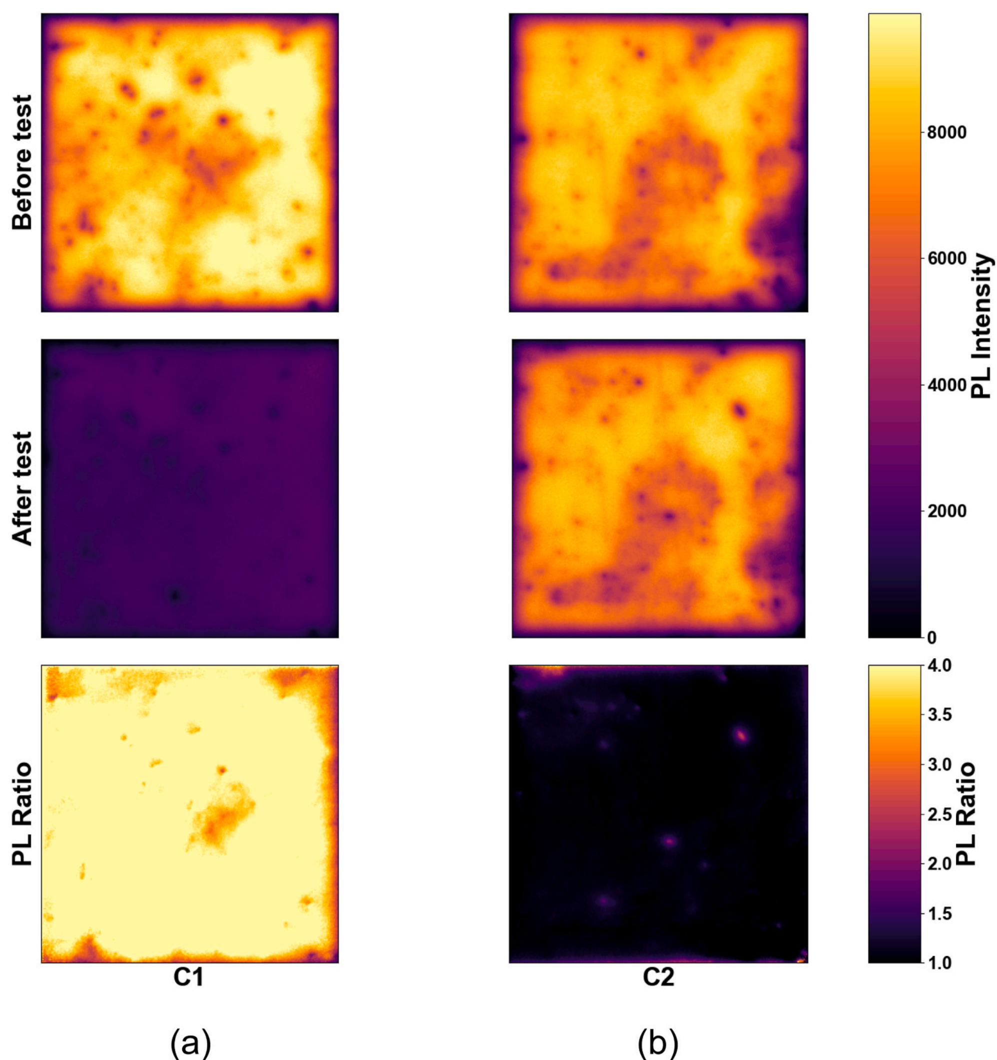

Fig. 6. The PL images of Group C after: (a) 20 h of UV exposure testing (C1); (b) 20 h of dark annealing (C2). Brighter regions in PL ratio images correspond to a greater reduction in PL intensity. The PL ratio is defined as $I_{PL,initial}/I_{PL,\ after\ treatment}$.

a factor of four. Under the low-injection conditions employed in the PL measurements, the PL intensity is directly linked to the effective carrier lifetime, and J_0 per side increased from 1.7 to 19.4 fA cm^2**.** This increase of approximately 18 fA cm^{-2} in J_0 is similar to the degradation observed at the rear surface of PERC cells and the front surface of TOPCon cells. In contrast, the samples subjected to dark annealing (C2) show negligible changes, indicating they are stable under this process.

As shown in Fig. 7 (a), the D_{it} of the as-received samples was at a

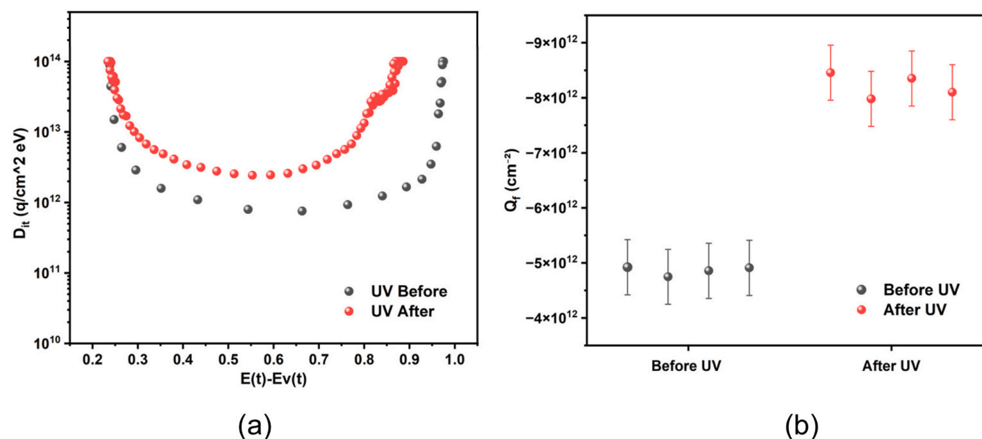

Fig. 7. Comparison of Group C samples before and after 20 h of UV irradiance: (a) evolution of the D_{it} data across the bandgap; (b) corresponding variations in the Q_f data of four samples.

relatively low level across the bandgap, particularly in the mid-gap region (~0.5–0.6 eV) with a D_{it} of ~8.0×10^{11} $cm^{-2}.eV^{-1}$. However, after 20 h of UVB exposure, a substantial increase in D_{it} is observed across the entire energy range, with the most pronounced rise occurring near the conduction-band edge and within the mid-bandgap region. In particular, the D_{it} near mid-gap increases to 2.4×10^{12} $cm^{-2}.eV^{-1}$, highlighting the formation of a significant density of mid-gap trap states. These mid-gap defects are particularly detrimental, as they serve as efficient non-radiative deep-level recombination centres, increasing carrier recombination rate and thereby reducing the minority carrier lifetime and degrading device performance. The increase in D_{it} after UVB irradiation thus directly reflects a deterioration in chemical passivation and an increased susceptibility to recombination-related losses. From Fig. 7 (b), the negative Q_f increased significantly following UVB irradiation, approximately doubling compared to its pre-irradiation value from around -5 to -8×10^{12} cm^{-2}. This rise in Q_f suggests improved field-effect passivation, which suppresses surface recombination by repelling minority carriers from the interface. However, the corresponding PL image (Fig. 6) shows a clear overall decrease in PL intensity, indicating increased carrier recombination. As a result, the overall passivation quality deteriorates, leading to lower carrier lifetimes and degraded device performance, even though the field-effect contribution becomes stronger.

The observed increase in D_{it} can probably attributed to UV-induced breaking of chemical bonds Si–H at or near the AlO_x/c-Si interface. The disruption of Si–H bond can result in the formation of silicon dangling bonds and increase the concentration of mobile hydrogen, which both increase the defect density at the AlO_x/c-Si interface and contribute to enhanced carrier recombination, as reported in the literature, including our earlier work [4], [18]. Meanwhile, the increase in Q_f is primarily associated with charge trapping and detrapping processes [20]. This process explains the observed increase in Q_f and the corresponding enhancement of the field-effect passivation after UV exposure. Moreover, the trapping process is reversible, de-trapping is believed to occur through electron tunnelling across the ultrathin interfacial oxide, followed by recombination with holes at the interface [20], [29]. While the present study focuses on AlO_x-only structures to isolate the intrinsic UV response of the AlO_x/c-Si interface, previous studies have reported that AlO_x/SiN_x stack samples incorporating a SiN_x capping layer exhibit stable effective lifetime under UVA illumination [4], [21]. Building on these findings, future work will extend this analysis to AlO_x/SiN_x stacks and device-relevant structures to assess how SiN_x modifies the observed degradation pathways under UVA and UVB exposure.

3.3. Theoretical modelling to understand UVID root cause

For silicon wafers passivated with an AlO_x layer, defects are inevitably present at the AlO_x/c-Si interface. These defects introduce energy levels within the silicon bandgap, acting as effective recombination centres that can severely limit the minority carrier lifetime of the c-Si wafer. The effectiveness of these recombination centres is governed by the Shockley-Read-Hall (SRH) model. According to this model, the lifetime of minority carriers (τ_{SRH}) is inversely proportional to the density of trap states (N_t) and their capability to capture electrons and holes. A larger capture cross-section can increase carrier recombination, thereby reducing carrier lifetime. This part compiles a comprehensive set of electrons (σ_n) and holes (σ_p) capture cross-section data from published literature, which are plotted as discrete points in Fig. 8 (a). The similar capture cross sections points reported for AlO_x and SiO_x in the literature can be explained by the formation of a thin interfacial SiO_x layer at the c-Si/AlO_x interface [34], [32]. A key observation from this dataset is the profound asymmetry between the two, with the ratio of hole-to-electron capture cross-sections (σ_p/σ_n) spanning a wide range [30]. To quantitatively model their energy distribution within the bandgap, we have represented these capture cross-sections using Gaussian functions [35], [32].

The capture cross sections were modelled using Gaussian functions, expressed as:

$$\sigma_{n/p} = \sigma_0 \exp\left[-A(E - E_0)^2\right] \tag{9}$$

The results of this fitting are shown in Fig. 8 (a), where the solid and dashed lines correspond to the modelled hole and electron capture cross-sections before and after UV exposure, respectively. The derived Gaussian functional models for the capture cross-sections are subsequently implemented within our numerical lifetime simulation framework. In this context, these functions provide a continuous, energy-dependent definition for $\sigma_n(E)$ and $\sigma_p(E)$, serving as the input parameters for the theoretical simulation.

To model the lifetime, we fit the energy dependence of the D_{it} using Gaussian distributions with exponential tails (for the band edges). A satisfactory fit cannot be achieved with one Gaussian distribution and two tails, and thus we fit the D_{it} with three Gaussian distributions and two tails, as illustrated in Fig. 8(b) and (c). The Gaussian distribution of the capture cross section is then adjusted until the simulated lifetime fits the measured lifetime of the symatrically passivated wafer as shown in Fig. 8 (d). The simulations were performed by numerically evaluating the SRH recombination rate at each energy level using the fitted D_{it} (E), capture cross sections, and the entire simulation workflow was implemented in Python. The corresponding Gaussian fitting parameters of D_{it} are summarized in **Table I**, which provides a detailed comparison of the variations before and after UVB irradiance. Following UVB exposure, the defect density tails near the valence ($D_{it,v}$) and conduction ($D_{it,c}$) band edges are relatively stable, whereas the trap density near the mid-gap region ($D_{it,0g,2}$) increases significantly, from 9.96×10^{11} to 2.77×10^{12} $cm^{-2}.eV^{-1}$. This pronounced increase in mid-gap states indicates the generation of deep-level defects, which are commonly associated with silicon dangling bonds at the c-Si/dielectric interface and act as highly efficient recombination centres [4]. Furthermore, both the valence-band trap centre ($E_{v,trap}$) and the conduction-band trap centre ($E_{c,trap}$) shift deeper toward the mid-gap after UVB exposure. Such energy shifts suggest a transformation of initially shallow, band-edge-related states into energetically deeper, more recombination-active states. The simultaneous rounded distribution and increase in peak density further support the formation of additional defects rather than a broad spectrum of randomly distributed states. Overall, the pronounced increase in mid-gap defects suggests that UV irradiation generates many deep-level defects acting as central recombination centres, thereby severely reducing carrier lifetime.

The theoretical lifetime fitting curves in Fig. 8 (d) were used to reproduce the experimental results of Group C. The methodology and parameters used to model effective lifetime is described in the **Appendix**. Although determining the absolute values of $\sigma_n(E)$, $\sigma_p(E)$, D_{it} and interfacial charges is challenging, it is feasible to monitor their relative variations during UV treatment, assuming that the intrinsic defect parameters remain constant and only the capture cross section, the charge states, and defect densities evolve [36]. Under this assumption, the fitted curves in Fig. 8 (d) capture the progressive modification of the interface properties induced by UVB irradiation. In our simulations, the effective charge **(Q_{fix})** primarily controls the low-injection lifetime through the surface potential and the resulting $\frac{n_s}{p_s}$, whereas the mid-gap D_{it} largely governs the overall magnitude of the lifetime across the full injection range by strengthening SRH recombination [36].

In Fig. 8 (d), the fitted lifetime curves are generated using the Q_{fix} values extracted from the experimental data, and mid-gap D_{it} parameters from three-peak Gaussian distribution modelling. While the COCOS measurement allows for the extraction of the impact of UV on charge and D_{it}, the lifetime modelling allows for the capture of potential changes in the electron and hole capture cross sections after UV exposure. In the simulation, the capture cross sections are modelled using a band-gap-dependent Gaussian distribution, as given by Eq. (9), and their

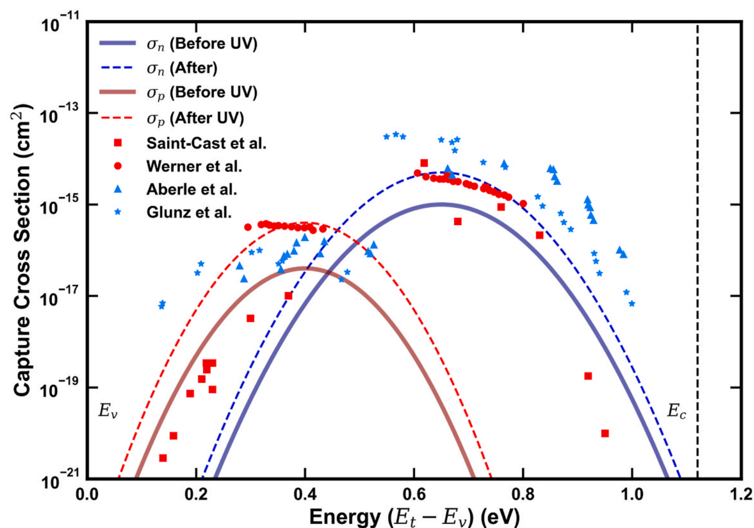

(a)

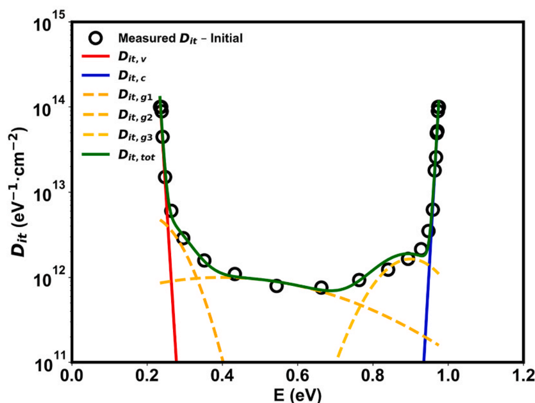

(b)

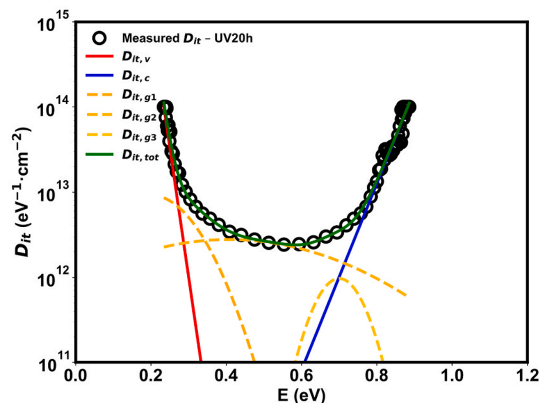

(c)

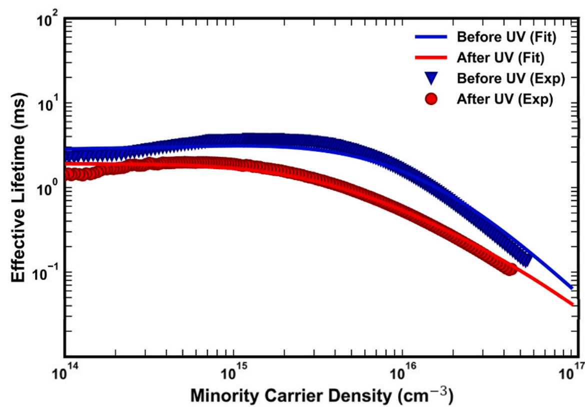

(d)

Fig. 8. (a) The Gaussian distribution comparison of capture cross sections (scatter data of the red color is AlO_x and the blue color is SiO_x) of electrons and holes under UV exposure [30], [31], [32], [33]; Gaussian modelling of D_{it} distribution versus energy with three interface defect distributions: (b) before UV irradiance, (c) after UV irradiance; (d) injection-dependent minority carrier lifetime before and after UV irradiance. (For interpretation of the references to color in this figure legend, the reader is referred to the Web version of this article.)

Table 1
The parameters of D_{it} three-peak gaussian-modelling fitting.

Parameters	Before UV	After UV
$D_{it,0v}(cm^{-2}.eV^{-1})$	1.24×10^{14}	1.01×10^{14}
$D_{it,0c}(cm^{-2}.eV^{-1})$	1.14×10^{14}	1.10×10^{14}
$D_{it,0g,1}(cm^{-2}.eV^{-1})$	5.28×10^{12}	9.16×10^{12}
$E_{0,1}(eV)$	0.2	0.2
$\sigma_1(eV^{\frac{1}{2}})$	0.072	0.092
$D_{it,0g,2}(cm^{-2}.eV^{-1})$	9.96×10^{11}	2.77×10^{12}
$E_{0,2}(eV)$	0.4	0.407
$\sigma_2(eV^{\frac{1}{2}})$	0.3	0.27
$D_{it,0g,3}(cm^{-2}.eV^{-1})$	1.64×10^{12}	9.66×10^{11}
$E_{0,3}(eV)$	0.9	0.7
$\sigma_3(eV^{\frac{1}{2}})$	0.084	0.055
$E_{v,trap}(eV)$	0.006	0.014
$E_{c,trap}(eV)$	0.006	0.04

variation is shown in Fig. 8 (a). After UV exposure, both the electron and hole capture cross sections increase markedly, with the peak electron capture cross section increasing by approximately a factor of five and the peak hole capture cross section increasing by nearly one order of magnitude. Despite this pronounced increase in magnitude, the Gaussian energy distribution of the capture cross sections within the bandgap remains largely unchanged. Together with the experimentally observed increase in mid-gap D_{it} and Q_{fix}, these results indicate that UVB exposure not only generates additional interface defect states but also that these states have different electronic properties. Within the Shockley–Read–Hall (SRH) recombination framework [32], [37], the simultaneous increase in D_{it} and in capture cross sections leads to a significantly enhanced recombination probability at the c-Si/AlO_x. Such behaviour may arise from hydrogen-related depassivation, local bond rearrangement, or a shift in the relative contribution of multiple interface-state species at the c-Si/AlO_x interface [38], [4]. UV exposure leads to simultaneous increases in mid-gap interface defect density, fixed charge, and capture cross-sections, which collectively enhance recombination activity at the c-Si/AlO_x interface. J_0 changes after UV exposure, extracted from the lifetime samples, remain lower than those typically extracted from solar cells, as expected, because the lifetime samples use undiffused wafers, whereas practical devices contain heavily diffused regions. To explain this, we use our extracted parameters on undiffused samples to model the impact of UV on diffused samples. Here, J_{0S} is the surface J_0 and excludes Auger recombination within the diffused emitter. Using these parameters measured on undiffused wafers passivated with AlO_x layer, we can extrapolate the impact of UVID on diffused surfaces passivated with AlO_x layer. Simulating this shows that the impact of UVID on diffused surfaces leads to a significantly higher increase in J_{0S} than in undiffused wafers as was experimentally shown by Khan et al. [4]. This is driven by two factors, 1) the gains from enhanced charge counterbalance increase D_{it} in undiffused wafers, do not translate to diffused wafers where the field effect passivation is already dominated by the emitter [39]; 2) the increase in D_{it} is higher near the band edges which leads to a higher impact on diffused surfaces. Note that we cannot simulate the cells measured above, as they were not synthetising in a similar way, thought the principles holds.

This observation may act in parallel with the hydrogen-accumulation hypothesis proposed by Khan et al. , where hydrogen released from the SiN_x:H layer under UV exposure redistributes towards the c-Si/dielectric interface [4], [18]. Such hydrogen redistribution may modify both the density and activity of interface states, potentially enhancing the recombination sensitivity of device structures compared with simplified lifetime samples. Additional modelling shows that increasing surface doping strongly amplifies the recombination penalty, indicating that the same UVID would lead to significantly larger J_0 increases in diffused structures. This is consistent with the degradation observed in PERC and TOPCon cells, where the AlOx/c-Si interface is present at the rear and front surfaces, respectively.

4. Conclusion

This work reveals UVID in silicon solar cells originates from degradation of the c-Si/dielectric passivation interface when it is directly exposed to UVB irradiation. Photoluminescence imaging of industrial solar cells shows a pronounce reduction in PL intensity (and increase in J_0) on both the front and rear surfaces of PERC cells, and also on the front surface of TOPCon cells as a result of UVB irradiation. In contrast, dark annealing produces negligible change. The rear side of TOPCon cells remains unaffected due to the presence of the n-poly layer, which absorbs the incident UV photons before they can reach in the c-Si interface. Both the front and rear surfaces of PERC cells exhibit UVID; however, the degradation is more pronounced on the front side. To isolate the physics of the c-Si/AlO_x interface, we investigate industrially fired AlO_x-passivated lifetime wafers without a SiN_x:H capping layer. Under the same UVB dose, the lifetime structures show a fourfold drop in PL intensity and a tenfold increase in J_0, with negligible changes for dark annealing. The lifetime structure degrades similarly to the cells.

Previous studies have attributed UVID to hydrogen related process (UV driven Si-H bond breaking and hydrogen redistribution) together with photon induced charging in the dielectric layers. Our observation is consistent with these studies. Our key contribution is that we resolve the energy dependence of the $D_{it}(E)$ and quantify how its evolution competes with the concurrent increase in Q_f. We show that both $D_{it}(E)$ and Q_f increase after UVID, with $D_{it}(E)$ increasing more strongly near the band-edges. Our fitting results suggest that the newly created defects have a larger capture cross section. Although more negative charge increases field effect passivation, its increase is not sufficient to offset the increase in D_{it} and capture cross section. The net result of the increase in D_{it} and charge is an increase in surface recombination as observed in both lifetime structures and cells.

One key implication of our results is that undiffused surfaces are expected to be more resilient than diffused surfaces under the same UVB treatment. This is explained two-fold: 1) The higher increase in $D_{it}(E)$ near the band edges, is likely to lead to greater recombination in diffused region 2) While on an undiffused surface, an increase in fixed charge (Q_f) can substantially enhance band bending (field effect passivation) and thus compensates the loss in chemical passivation from increase in D_{it}, on a diffused surface, a significant fraction of the field effect passivation is already provided by the diffusion itself and thus an increase charge produces a smaller band bending and thus smaller increase in field effect passivation. The impact of D_{it} thus more readily dominates the recombination activity leading to greater increase in J_0. This observation is consistent with cells measurements showing higher degradation on diffused surfaces.

CRediT authorship contribution statement

Jiaxin Yang: Data curation, Formal analysis, Investigation, Methodology, Writing – original draft. **Muhammad Umair Khan:** Resources, Writing – review & editing. **Xinyuan Wu:** Conceptualization, Resources, Validation. **Chandany Sen:** Resources, Validation. **Jessica Yajie Jiang:** Resources, Validation. **Bram Hoex:** Investigation, Methodology, Resources, Validation, Writing – review & editing. **Fiacre Rougieux:** Conceptualization, Investigation, Methodology, Resources, Supervision, Validation, Writing – review & editing.

Declaration of competing interest

The authors declare that they have no known competing financial interests or personal relationships that could have appeared to influence the work reported in this paper.

Acknowledgements

This work was supported by the Australian Centre for Advanced Photovoltaics (ACAP), funded by the Australian Government through the Australian Renewable Energy Agency (ARENA). The views, information, and advice expressed in this publication are those of the authors and do not necessarily reflect the views of the Australian Government. The authors would like to thank the SLDOT team at SPREE, UNSW, both at TETB and SIRF, for their dedicated support in maintaining laboratory health and safety standards and ensuring the smooth operation of the facilities, which greatly enabled the successful execution of this work. Furthermore, Jiaxin Yang acknowledges the support received from the Australian Government Research Training Program (RTP) Scholarship.

Appendix

For the theoretical simulation of carrier lifetime, we primarily employed the equation for effective lifetime, which is given as follows:

$$\frac{1}{\tau_{eff}} = \frac{1}{\tau_{int}} + \frac{1}{\tau_{bulk}} + \frac{1}{\tau_{surf}} \tag{A1}$$

Among them, τ_{int} denotes the intrinsic lifetime, which includes both Auger and radiative recombination; τ_{bulk} represents the bulk SRH lifetime; and τ_{surf} refers to the surface lifetime. To simulate the surface recombination rate, we replace N_t with D_{it}, and calculate the recombination rate (R) through integration over the entire energy band, which can be obtained [40]:

$$R = \int_{Ev}^{E_c} \frac{v_{th}\left(n_s p_s - n_{i,eff}^2\right) D_{it}(E) dE}{\frac{n_s + n_1(E)}{\sigma_p(E)} + \frac{p_s + p_1(E)}{\sigma_n(E)}} \tag{A2}$$

Where v_{th} is the thermal velocity, n_s and p_s are the carrier concentration near the surface, and n_i means the intrinsic carrier concentration. The parameters $p_1(E)$ and $n_1(E)$ represent the thermal emission rates of holes and electrons from the defect energy level, respectively. Accordingly, we employ the $D_{it}(E)$ parameter obtained through Gaussian simulation in the recombination rate formula to evaluate R, which is then used to derive τ_{surf}. $\sigma_p(E)$ and $\sigma_n(E)$ can used Eq. (9). Thus, the wafer lifetime is theoretically calculated using the D_{it} model and subsequently fitted and compared with the experimentally obtained lifetime data.

The parameters of $p_1(E)$ and $n_1(E)$ can be calculated by:

$$n1 = N_c \exp\left(-\frac{E_c - E_t}{kT}\right), p1 = N_v \exp\left(-\frac{E_t - E_v}{kT}\right) \tag{A3}$$

The term of n_s and p_s can be described as:

$$n_s = n_d \, exp\left(-\frac{\psi_s}{kT}\right), p_s = p_d \, exp\left(\frac{\psi_s}{kT}\right) \tag{A4}$$

The study by *Xin* et al. proposes an advanced method for extracting D_{it}, which models the characteristic U-shaped distribution by fitting a composite function [41]. This function comprises a Gaussian distribution representing the central bond-deficiency-related defects and two exponential tail distributions accounting for the band-edge localized states [32]. Such an approach enables more accurate characterization of the defect profile across the silicon bandgap. The distribution of Gaussian defect distribution near the mid-band gap, along with defect states near the conduction and valence band edges, often deviates from ideal crystal symmetry. These deviations can be effectively described using exponential tail states, as formulated in Eqs. (A5) - (A8):

$$D_{it,v}(E) = D_{it,0v} \times e^{\frac{E_v - E}{E_{v,trap}}} \tag{A5}$$

$$D_{it,c}(E) = D_{it,0c} \times e^{\frac{E - E_c}{E_{c,trap}}} \tag{A6}$$

$$D_{it,g}(E) = D_{it,0g} \times e^{-\frac{1}{2}\left(\frac{E - E_0}{\sigma}\right)^2} \tag{A7}$$

$$D_{it,tot}(E) = D_{it,v}(E) + D_{it,c}(E) + D_{it,g}(E) \tag{A8}$$

Data availability

Data will be made available on request.

References

[1] F. T. Thome et al., "UV-Induced degradation of industrial PERC, TOPCon, and HJT solar cells: the next big reliability challenge?," Sol. RRL, vol. 8, no. 23, p. 2400628, doi: 10.1002/solr.202400628.

[2] Z. Li, et al., UVID of TOPCon solar cells: effect of the front passivation Al2O3 layer thickness and recovery by different processes, Sol. Energy Mater. Sol. Cells 289 (Aug. 2025) 113691, https://doi.org/10.1016/j.solmat.2025.113691.

[3] S. Razzaq, et al., Enhancing UV light stability in commercial silicon HJT solar cells and modules, Sol. Energy 298 (Sep. 2025) 113735, https://doi.org/10.1016/j.solener.2025.113735.

[4] M.U. Khan, et al., UV-induced degradation in TOPCon solar cells: hydrogen dynamics and impact of UV wavelength, Sol. Energy Mater. Sol. Cells 294 (Jan. 2026) 113895, https://doi.org/10.1016/j.solmat.2025.113895.

[5] "Kiwa PVEL PV module reliability scorecard," 2025 module scorecard [Online]. Available: https://scorecard.pvel.com/. (Accessed 29 April 2026).

[6] E. Klampaftis, D. Ross, K.R. McIntosh, B.S. Richards, Enhancing the performance of solar cells via luminescent down-shifting of the incident spectrum: a review, Sol. Energy Mater. Sol. Cells 93 (8) (Aug. 2009) 1182–1194, https://doi.org/10.1016/j.solmat.2009.02.020.

[7] "Shedding light on ultraviolet-induced degradation," RETC, LLC [Online]. Available: https://retc-ca.com/news/shedding-light-on-ultraviolet-induced-degradation. (Accessed 14 October 2025).
[8] A. Mayavan, Comprehensive review on downconversion/downshifting silicate-based phosphors for solar cell applications, ACS Omega 9 (15) (Apr. 2024) 16880–16892, https://doi.org/10.1021/acsomega.3c08806.
[9] "Uvid," 2025 module scorecard [Online]. Available: https://scorecard.pvel.com/uvid/. (Accessed 14 October 2025).
[10] F. Ye, et al., UV-induced degradation in multicrystalline PERC cell and module, Sol. Energy 170 (Aug. 2018) 1009–1015, https://doi.org/10.1016/j.solener.2018.06.044.
[11] R. Witteck, et al., UV-induced degradation of PERC solar modules with UV-transparent encapsulation materials, Prog. Photovoltaics Res. Appl. 25 (6) (2017) 409–416, https://doi.org/10.1002/pip.2861.
[12] A. Sinha, K. Hurst, S. Uličná, L.T. Schelhas, D.C. Miller, P. Hacke, Assessing UV-Induced degradation in bifacial modules of different cell technologies, in: 2021 IEEE 48th Photovoltaic Specialists Conference (PVSC), Jun. 2021, pp. 767–770, https://doi.org/10.1109/PVSC43889.2021.9518728.
[13] A. Sinha, et al., UV-induced degradation of high-efficiency silicon PV modules with different cell architectures, Prog. Photovoltaics Res. Appl. 31 (1) (2023) 36–51, https://doi.org/10.1002/pip.3606.
[14] M.F. Azam, N. Shahzad, A. Rafique, M. Ayub, H. Abdullah Khalid, A. Waqas, Accelerated UV stress testing and characterization of PV-modules: reliability analysis using different encapsulants and glass sheets, Sustain. Energy Technol. Assessments 56 (Mar. 2023) 103119, https://doi.org/10.1016/j.seta.2023.103119.
[15] J. Yang, et al., Unveiling the mechanism of ultraviolet-induced degradation in silicon heterojunction solar cells, Sol. Energy Mater. Sol. Cells 276 (Oct. 2024) 113062, https://doi.org/10.1016/j.solmat.2024.113062.
[16] J. Ren, et al., Predicting the lifetime of HJT modules towards the outdoor real-world environment, Sol. Energy Mater. Sol. Cells 272 (Aug. 2024) 112885, https://doi.org/10.1016/j.solmat.2024.112885.
[17] H. Ye, et al., Short wavelength photons destroying Si–H bonds and its influence on high-efficiency silicon solar cells and modules, Sol. RRL 7 (15) (2023) 2300334, https://doi.org/10.1002/solr.202300334.
[18] M.U. Khan, et al., Charge trapping, hydrogen accumulation, and structural rearrangement: a complete model for ultraviolet-induced degradation in TOPCon devices, Sol. Energy Mater. Sol. Cells 298 (May 2026) 114149, https://doi.org/10.1016/j.solmat.2025.114149.
[19] R. Witteck, et al., UV radiation hardness of photovoltaic modules featuring crystalline si solar cells with AlOx/p++-type si and SiNy/n+-type si interfaces, Phys. Status Solidi RRL 11 (8) (2017) 1700178, https://doi.org/10.1002/pssr.201700178.
[20] J.J.H. Gielis, B. Hoex, M.C.M. Van De Sanden, W.M.M. Kessels, Negative charge and charging dynamics in Al2O3 films on Si characterized by second-harmonic generation, J. Appl. Phys. 104 (7) (Oct. 2008) 073701, https://doi.org/10.1063/1.2985906.
[21] B. Veith-Wolf, R. Witteck, A. Morlier, H. Schulte-Huxel, J. Schmidt, Effect of UV illumination on the passivation quality of AlOx/c-Si interfaces, in: 2016 IEEE 43rd Photovoltaic Specialists Conference (PVSC), Jun. 2016, pp. 1173–1178, https://doi.org/10.1109/PVSC.2016.7749799.
[22] D.N.R. Payne, C. Vargas, Z. Hameiri, S.R. Wenham, D.M. Bagnall, An advanced software suite for the processing and analysis of silicon luminescence images, Comput. Phys. Commun. 215 (Jun. 2017) 223–234, https://doi.org/10.1016/j.cpc.2017.02.012.
[23] H. Nagel, C. Berge, A.G. Aberle, Generalized analysis of quasi-steady-state and quasi-transient measurements of carrier lifetimes in semiconductors, J. Appl. Phys. 86 (11) (Dec. 1999) 6218–6221, https://doi.org/10.1063/1.371633.
[24] A. Richter, F. Werner, A. Cuevas, J. Schmidt, S.W. Glunz, Improved parameterization of auger recombination in silicon, Energy Proc. 27 (Jan. 2012) 88–94, https://doi.org/10.1016/j.egypro.2012.07.034.
[25] M. Wilson, J. Lagowski, A. Savtchouk, L. Jastrzebski, J. D'Amico, COCOS (corona oxide characterization of semiconductor) metrology: physical principles and applications, in: Gate Dielectric Integrity: Material, Process, and Tool Qualification, ASTM International, 2000, pp. 74–90 [Online]. Available: https://dl.astm.org/stps/book/chapter-pdf/59157/10_1520_stp13485s.pdf. (Accessed 29 April 2026).
[26] R. Bhoopathy, O. Kunz, M. Juhl, T. Trupke, Z. Hameiri, Outdoor photoluminescence imaging of solar panels by contactless switching: technical considerations and applications, Prog. Photovoltaics Res. Appl. 28 (3) (Mar. 2020) 217–228, https://doi.org/10.1002/pip.3216.
[27] A. Cuevas, The recombination parameter J0, Energy Proc. 55 (Jan. 2014) 53–62, https://doi.org/10.1016/j.egypro.2014.08.073.
[28] A. Cuevas, D. Macdonald, Measuring and interpreting the lifetime of silicon wafers, Sol. Energy 76 (1) (Jan. 2004) 255–262, https://doi.org/10.1016/j.solener.2003.07.033.
[29] B. Liao, R. Stangl, T. Mueller, F. Lin, C.S. Bhatia, B. Hoex, The effect of light soaking on crystalline silicon surface passivation by atomic layer deposited Al2O3, J. Appl. Phys. 113 (2) (Jan. 2013) 024509, https://doi.org/10.1063/1.4775595.
[30] P. Saint-Cast, et al., Variation of the layer thickness to study the electrical property of PECVD Al2O3/c-Si interface, Energy Proc. 8 (Jan. 2011) 642–647, https://doi.org/10.1016/j.egypro.2011.06.195.
[31] A.G. Aberle, S.W. Glunz, A.W. Stephens, M.A. Green, High-eficiency silicon solar cells: Si/SiO2, interface parameters and their impact on device performance, Prog. Photovoltaics Res. Appl. 2 (4) (1994) 265–273, https://doi.org/10.1002/pip.4670020402.
[32] F. Werner, A. Cosceev, J. Schmidt, Interface recombination parameters of atomic-layer-deposited Al2O3 on crystalline silicon, J. Appl. Phys. 111 (7) (Apr. 2012) 073710, https://doi.org/10.1063/1.3700241.
[33] X. Tan, R. Chen, F.E. Rougieux, The mechanism of surface passivation degradation in SiO2/SiNx stack under light and elevated temperature, IEEE J. Photovoltaics 11 (6) (Nov. 2021) 1380–1387, https://doi.org/10.1109/JPHOTOV.2021.3106881.
[34] B. Hoex, S.B.S. Heil, E. Langereis, M.C.M. van de Sanden, W.M.M. Kessels, Ultralow surface recombination of c-si substrates passivated by plasma-assisted atomic layer deposited Al2O3, Appl. Phys. Lett. 89 (4) (Jul. 2006) 042112, https://doi.org/10.1063/1.2240736.
[35] D. Schuldis, A. Richter, J. Benick, P. Saint-Cast, M. Hermle, S.W. Glunz, Properties of the c-si/Al2O3 interface of ultrathin atomic layer deposited Al2O3 layers capped by SiNx for c-si surface passivation, Appl. Phys. Lett. 105 (23) (Dec. 2014) 231601, https://doi.org/10.1063/1.4903483.
[36] F.E. Rougieux, C. Sen, M. Abbott, B. Hoex, Light-activated surface passivation for more efficient silicon heterojunction solar cells: origin, physics and stability, Sol. Energy Mater. Sol. Cells 269 (Jun. 2024) 112789, https://doi.org/10.1016/j.solmat.2024.112789.
[37] R.B.M. Girisch, R.P. Mertens, R.F. De Keersmaecker, Determination of si-SiO/sub 2/interface recombination parameters using a gate-controlled point-junction diode under illumination, IEEE Trans. Electron. Dev. 35 (2) (Feb. 1988) 203–222, https://doi.org/10.1109/16.2441.
[38] L.E. Black, K.R. McIntosh, Modeling recombination at the si–Al_2O_3 interface, IEEE J. Photovoltaics 3 (3) (Jul. 2013) 936–943, https://doi.org/10.1109/JPHOTOV.2013.2247464.
[39] K.R. McIntosh, L.E. Black, On effective surface recombination parameters, J. Appl. Phys. 116 (1) (Jul. 2014) 014503, https://doi.org/10.1063/1.4886595.
[40] W.D. Eades, R.M. Swanson, Calculation of surface generation and recombination velocities at the Si-SiO2 interface, J. Appl. Phys. 58 (11) (Dec. 1985) 4267–4276, https://doi.org/10.1063/1.335562.
[41] Z. Xin, et al., An improved methodology for extracting the interface defect density of passivated silicon solar cells, IEEE J. Photovoltaics 6 (5) (Sep. 2016) 1080–1089, https://doi.org/10.1109/JPHOTOV.2016.2576685.